論文 / 著書情報
Article / Book Information

Title	Truly chiral phonons in α-HgS
Authors	Kyosuke Ishito, Huiling Mao, Yusuke Kousaka, Yoshihiko Togawa, Satoshi Iwasaki, Tiantian Zhang, Shuichi Murakami, Jun-ichiro Kishine, Takuya Satoh
Citation	Nature Physics, Vol. 19, Issue 1, pp. 35-39
Pub. date	2023, 1
note	The version of record of this article, first published in Nature Physics, is available online at Publisher ' s website: https://dx.doi.org/10.1038/s41567-022-01790-x
Creative Commons	Information is in the article.

nature physics

Letter

https://doi.org/10.1038/s41567-022-01790-x

Truly chiral phonons in α-HgS

Received: 30 September 2021

Accepted: 5 September 2022

Published online: 31 October 2022

Check for updates

Kyosuke Ishito[1,7], Huiling Mao[1,7], Yusuke Kousaka[2,3], Yoshihiko Togawa[2], Satoshi Iwasaki[3], Tiantian Zhang[1,4], Shuichi Murakami[1,4], Jun-ichiro Kishine[5,6] & Takuya Satoh[1]

Chirality is a manifestation of the asymmetry inherent in nature. It has been defined as the symmetry breaking of the parity of static objects, and the definition was extended to dynamic motion such that true and false chiralities were distinguished. Recently, rotating, yet not propagating, atomic motions were predicted and observed in two-dimensional materials, and they were referred to as 'chiral phonons'. A natural development would be the discovery of truly chiral phonons that propagate while rotating in three-dimensional materials. Here we used circularly polarized Raman scattering and first-principles calculations to identify truly chiral phonons in chiral bulk crystals. This approach enabled us to determine the chirality of a crystal in a non-contact and non-destructive manner. In addition, we demonstrated that the law of the conservation of pseudo-angular momentum holds between circularly polarized photons and chiral phonons. These findings are expected to help develop ways for transferring the pseudo-angular momentum from photons to electron spins via propagating chiral phonons in opto-phononic-spintronic devices.

Chirality, the breaking of reflection and inversion symmetries[1], appears at all levels of nature and has been studied in many fields of research[2]. Barron extended the concept of chirality to the dynamic regime by classifying into true and false chiralities[3]. True chirality is demonstrated by systems that exist in two different enantiomeric states that are interconverted by spatial inversion ($\mathcal{P}$), rather than by time inversion ($\mathcal{T}$) combined with appropriate spatial rotation ($\mathcal{R}$) (ref. 3). This concept contrasts with false chirality, where the two states are interconverted by $\mathcal{P}$ and by $\mathcal{T}$, for example, magneto-optical Faraday rotation.

Chirality was further extended to the dynamics of quasi-particles. Possible band structure shapes have been classified in terms of pseudo-momentum and pseudo-angular momentum (PAM)[4], which originate from the phase factors acquired by discrete translation and rotation symmetry operations on wave functions, respectively. In crystals, these are different from the momentum and angular momentum (AM), which are continuous linear and circular motions of an object in real space, respectively. Recently, circularly rotating atomic motion with non-zero PAM and AM at high-symmetry points in the Brillouin zone in monolayer hexagonal lattices was theoretically predicted and named 'chiral phonons,[5,6]. This prediction was verified experimentally in the transition-metal dichalcogenide WSe_2 via transient infrared spectroscopy[7].

Employing Barron's true chirality, one can extend the concept of a chiral phonon to 'truly chiral phonons', which have two enantiomeric chiral modes that propagate with finite group velocity while circularly rotating in three-dimensional materials wherein PAM and AM have opposite signs. These modes should be interconverted by $\mathcal{P}$ but not by $\mathcal{RT}$. The observation of truly chiral phonons would require the use of chiral materials, as has been proposed theoretically[8]. Several Raman experiments designed to identify phonon symmetry in chiral crystals have been conducted[9–15]. Frequency-degenerated phonon modes were observed to undergo splitting at the centre of the Brillouin zone (Γ_3 doublets) in α-quartz and trigonal tellurium[9,11]. Moreover, theoretical work on phonon band dispersion has been reported on α-HgS (cinnabar), where the splitting was attributed to the linear wave vector shifts caused by chirality[16]. Nonetheless, previous studies have mostly

[1]Department of Physics, Tokyo Institute of Technology, Tokyo, Japan. [2]Department of Physics and Electronics, Osaka Metropolitan University, Osaka, Japan. [3]Research Institute for Interdisciplinary Science, Okayama University, Okayama, Japan. [4]Tokodai Institute for Element Strategy (TIES), Tokyo Institute of Technology, Tokyo, Japan. [5]Division of Natural and Environmental Sciences, The Open University of Japan, Chiba, Japan. [6]Institute for Molecular Science, Okazaki, Japan. [7]These authors contributed equally: Kyosuke Ishito and Huiling Mao. e-mail: satoh@phys.titech.ac.jp

https://doi.org/10.1038/s41567-022-01790-x

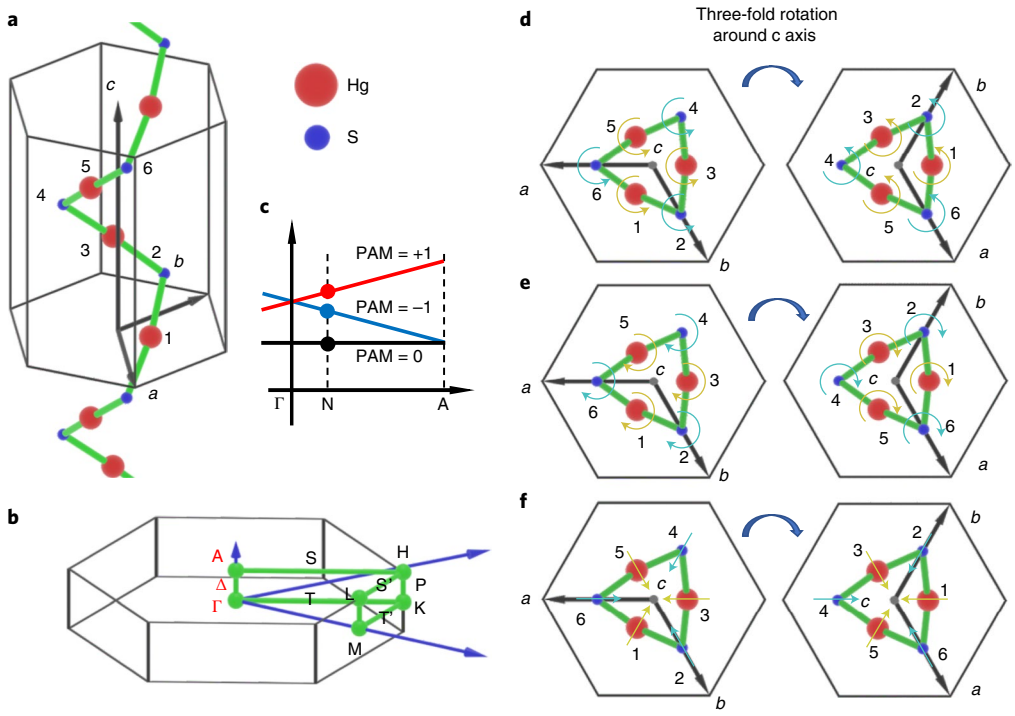

Fig. 1 | Chiral properties of α-HgS. a, Right-handed helical chain along the *c* axis of R-HgS. Each Hg atom (red sphere) is bonded with two S atoms (blue spheres). Chemical bonds are denoted by green lines. **b**, Brillouin zone of α-HgS. The blue lines indicate the reciprocal lattice vectors. The green lines and dots represent the high-symmetry paths and points, respectively. **c**, Schematic diagram of phonon dispersion from the Γ to A point. Filled red, blue and black circles at the N point correspond to the phonon modes of **d**, **e** and **f**, respectively. **d**–**f**, Two-dimensional projections of schematic atomic motions (Hg, gold arrows; S, blue arrows) in R-HgS at point N for a Δ_2 mode with $m^{s}_{PAM} = +1$ and $m_{AM} > 0$ (**d**), a Δ_3 mode with $m^{s}_{PAM} = -1$ and $m_{AM} < 0$ (**e**) and a Δ_1 mode with $m^{s}_{PAM} = 0$ and $m_{AM} \simeq 0$ (**f**). The black lines indicate the lattice vectors. Counter-clockwise, clockwise circular and linear motions indicate that m_{AM} is positive, negative and zero, respectively. The three-fold rotation symmetry operation generates phase factors of atomic motions, namely PAM m^{s}_{PAM}. The phase difference at the position of each atom after the operation is shown.

focused on examining the phonon symmetry without considering PAM and AM.

Here we used circularly polarized Raman spectroscopy (Methods) to observe the phonon modes and their splitting in chiral crystals of α-HgS. Moreover, we performed first-principles calculations (Methods) to compute the dispersion, PAM and AM of phonons in α-HgS. A comparison between the experiment and calculation shows that the split phonons were indeed truly chiral phonons. We also confirmed that the conservation law of PAM holds in circularly polarized Raman scattering by taking into account the three-fold rotational symmetry.

Trigonal α-HgS crystals contain two enantiomeric cinnabar structures with right- and left-handed helices (R- and L-HgS), which belong to the space groups $P3_121$ (translation by $c/3$ in three-fold rotation) and $P3_221$ (translation by $2c/3$ in three-fold rotation), respectively[17]. This crystal has a three-fold helical axis along the *c* direction (Fig. 1a), with large optical activity[18]. Our samples were single crystals of naturally grown α-HgS with lateral dimensions of 3 mm. We selected a *c*-axis-oriented as-grown surface of R-HgS, which was confirmed by X-ray analysis.

The phonon modes at the centre of the Brillouin zone (Γ point) of α-HgS are classified into two $\Gamma_1^{(1,2)}$ singlets (Raman active), three $\Gamma_2^{(1-3)}$ singlets (infrared active) and five $\Gamma_3^{(1-5)}$ doublets (Raman and infrared active). Our measurement led to the observation of the $\Gamma_1^{(1,2)}$ singlets and $\Gamma_3^{(2-5)}$ doublets, which were assigned on the basis of the selection rule[19] for the four incident/scattered polarization configurations (RR, LL, RL and LR), where $I_{RR}:I_{LL}:I_{RL}:I_{LR} = 1:1:0:0$ and $0:0:1:1$ for the Γ_1 and Γ_3 modes, respectively (Extended Data Fig. 1). The transverse optical (TO) phonons of the Γ_3 mode were generated because the incident and scattered light were propagated along the *c* axis. A weak signal was detected for the longitudinal optical (LO) phonon at ~145 cm^{-1}, presumably owing to misalignment of the experimental setup.

The phonon frequencies obtained by the Raman experiment are compared with the results of the first-principles calculations and with previous results[10,16] in Extended Data Table 1. The results of the Raman experiments both of our study and of a previous study[10] are identical to within 3 cm^{-1}. The results of our calculations at the Γ point also closely approximate those in ref. 16, and the small differences are attributed to the difference in the positions of the atoms. In our experiments, the $\Gamma_3^{(1)}$ mode was not observed because this mode is nearly degenerate with the $\Gamma_1^{(1)}$ mode, which has a much higher intensity. In Extended Data Table 1, the frequencies of the $\Gamma_3^{(2-5)}$ modes obtained in our Raman experiment are averaged for the RL and LR configurations, which were split as shown in the next paragraph.

The Stokes and anti-Stokes Raman spectra (Raman optical activity) of each $\Gamma_3^{(2-5)}$ mode are shown in Fig. 2a–h. All four Γ_3 modes were observed with the opposite circularly polarized light between the incident and scattered light (RL and LR). On the anti-Stokes spectra (Fig. 2a–d), the absolute values of the Raman shift of the $\Gamma_3^{(2)}$ and $\Gamma_3^{(4)}$ modes in the RL configuration are lower than those in the LR configuration in Fig. 2a,c. In Fig. 2b,d, the absolute values of the Raman shift of the $\Gamma_3^{(3)}$ and $\Gamma_3^{(5)}$ modes in the RL configuration are higher than those in the LR configuration. On the Stokes spectra (Fig. 2e–h), the splittings are mirror images of those on the anti-Stokes spectra (Fig. 2a–d). The $\Gamma_1^{(1,2)}$ modes do not split.

The properties of phonons are discussed here on the basis of our first-principles calculations. Figure 3a displays the phonon dispersion curve calculated along the path Δ from the Γ to A point, which is parallel to the *c* axis (Fig. 1b). Linear splittings of $\Gamma_3^{(1-5)}$ modes appear around the Γ point, which is consistent with previous calculations[16,20]. From the conservation law of pseudo-momentum, the wavenumber *k* of phonons observed by backscattering Raman spectroscopy is expressed

https://doi.org/10.1038/s41567-022-01790-x

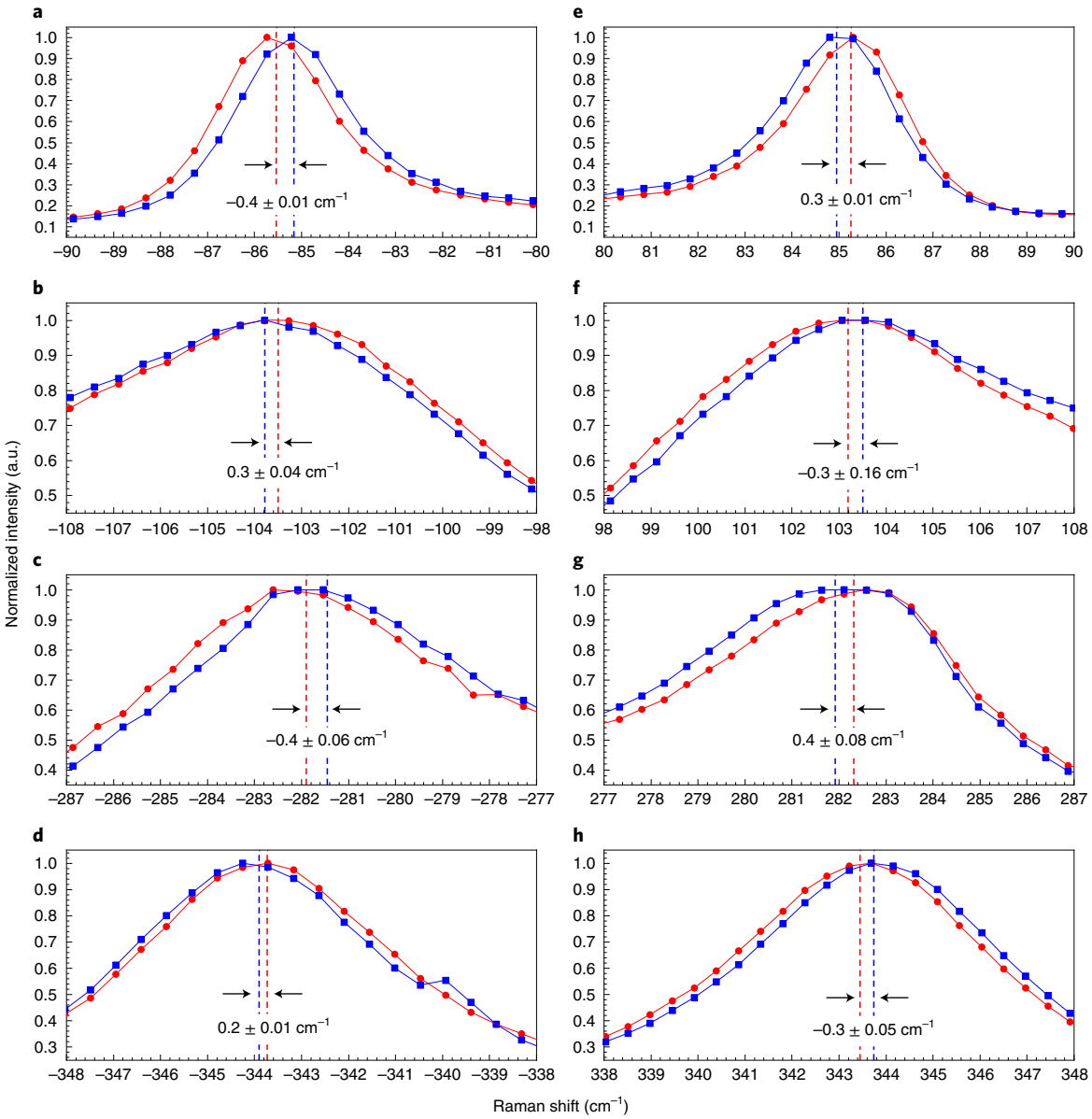

Fig. 2 | Raman spectra of R-HgS. a–h, Anti-Stokes (**a**–**d**) and Stokes (**e**–**h**) spectra of the $\Gamma_3^{(2)}$ (**a**,**e**), $\Gamma_3^{(3)}$ (**b**,**f**), $\Gamma_3^{(4)}$ (**c**,**g**) and $\Gamma_3^{(5)}$ (**d**,**h**) modes, along with the Γ_3 modes observed experimentally with RL- (blue line) and LR-polarized (red line) configurations and the Γ_3 doublet splittings (dashed vertical lines) in **a**–**h**. The error values take into account that multiple splitting measurements were conducted in the experiment, owing to the roughness of the sample surface.

as $k = 4\pi n/\lambda$, where λ is the wavelength of the incident or scattered light, and $n = 2.77$ is the absolute value of the complex refractive index of α-HgS[21]. The value of k was calculated to be ~1/80 of the wavenumber π/c at the A point. We denoted this specific point on the path Δ as 'N' in Fig. 3a. The experimental splitting values of the Γ_3 modes at this point (Stokes scattering) are almost consistent with the calculations (Extended Data Table 2). Therefore, we attribute the splits observed in Fig. 2 to the linear k shifts at the N point.

To understand the selection rule of the incident/scattered polarization configurations on the Raman spectra in Fig. 2, we calculated the PAM of phonons in R-HgS (Methods). As shown in Fig. 3a, the Γ_3 doublets have spin PAM $m^s_{PAM} = \pm 1$, whereas the Γ_1 and Γ_2 singlets have $m^s_{PAM} = 0$. The phonon bands with $m^s_{PAM} = -1$ and $m^s_{PAM} = 0$ intersect at the A point. These are the common features of the 3_1 (right-handed) helix[4,9,22]. From Figs. 2e–h and 3a, $\Gamma_3^{(2-5)}$ phonons with $m^s_{PAM} = +1$ and −1 were observed in the LR and RL configurations, respectively (Extended Data Table 2). Γ_1 phonons with $m^s_{PAM} = 0$ were observed in the RR and LL configurations. Right- and left-handed circularly polarized light possess PAM of $\sigma = +1$ and −1, respectively[23]. Therefore, we confirmed a conservation law to exist between the spin PAM of phonons and the PAM of the incident/scattered photons in the Stokes spectra as

$$\sigma_s - \sigma_i = -m^s_{PAM} + 3p, \quad (1)$$

where σ_s and σ_i represent the PAM of the scattered and incident photons, respectively. In addition, $p = 0$ and ±1 for the Γ_1 and Γ_3 modes, respectively. The factor $3p$ on the right-hand side of equation (1) can be understood by considering the three-fold rotational symmetry of α-HgS and the Umklapp process in Raman scattering[4,24–27].

In crystals with discrete rotational symmetry, a clear distinction should be made between the PAM and AM of the phonons. The AM of phonons arises from the circular vibration of atoms in the real space, as shown in Fig. 1d–f (see also Supplementary Videos 1 and 2). The AM of phonons along the c axis is displayed in Fig. 3b along with the

https://doi.org/10.1038/s41567-022-01790-x

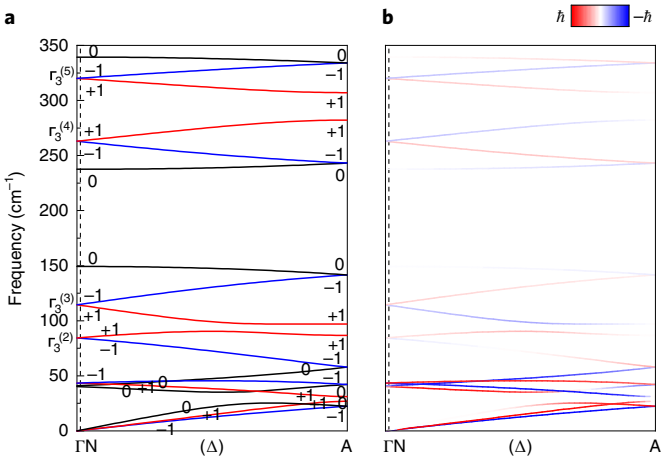

Fig. 3 | Dispersion of R-HgS along the right-handed helical axis. a, Phonon dispersion curves for spin PAM $m^{s}_{PAM} = 0$ (black), +1 (red) and −1 (blue). The wavenumbers at the N and A points are in the ratio of 1:80. **b**, Phonon AM along the helical axis, denoted by the colour gradient. Red and blue curves correspond to the positive and negative AM, respectively.

Γ to A point (Methods). In the vicinity of the Γ point, the Γ_3 modes have clockwise and counter-clockwise rotations, corresponding to the positive and negative AM of phonons, respectively. This is a clear manifestation of the existence of chiral phonons. The Γ_1 modes have linear vibrations, and their phonons have zero AM. The signs of AM at the N point are listed in Extended Data Table 2, where the spin PAM and AM of phonons do not correspond with each other. This indicates that, contrary to PAM, the AM of phonons is not conserved during the Raman process in a crystal with discrete rotational symmetry.

We also calculated the PAM and AM of phonons in L-HgS (Extended Data Fig. 2). The signs of the spin PAM and AM are reversed with respect to Fig. 3, that is, $m^{s}_{PAM}(RH, k, j) = -m^{s}_{PAM}(LH, k, j)$ and $m_{AM}(RH, k, j) = -m_{AM}(LH, k, j)$, where RH and LH denote crystals with right- and left-handed helices, respectively. This means that the splitting of the Γ_3 modes arises from chirality. From the first-principles calculation, the phonon eigenvector at the N point $\mathbf{u}(RH, k, j)$ and $\mathbf{u}(LH, k, j)$ are converted by $\mathcal{P}$, $\mathcal{T}$ and $\mathcal{C}_2$ as $\mathcal{P}\mathbf{u}(RH, k, j) = \mathbf{u}(LH, -k, j)$, $\mathcal{C}_2\mathcal{T}\mathbf{u}(RH, k, j) = \mathcal{C}_2\mathbf{u}(RH, -k, j) = \mathbf{u}(RH, k, j)$ where $\mathcal{C}_2$ is a two-fold rotation around the **a**, **b** or **a** + **b** direction. These relations satisfy the definition of true chirality with two different enantiomeric phonon modes: $\mathbf{u}(RH, k, j)$ and $\mathbf{u}(LH, -k, j)$.

We also recorded the Raman spectra of an α-HgS crystal for which the handedness (chirality) of the measured region was unknown because the size of the chiral domain was smaller than the experimental resolution (~1 mm) of our X-ray diffractometer. Contrary to the X-ray analysis, our Raman experiment with a spatial resolution of a few microns succeeded in observing the splitting of the Γ_3 modes (Extended Data Fig. 3), and the directions of the splittings were opposite to the results in Fig. 2. Considering the data in Extended Data Table 3, the chirality of the sample at the point of measurement was found to be left-handed.

Space group analysis enabled us to additionally assign an irreducible representation of the phonon dispersion curve in R-HgS. On path Δ from Γ to A, three irreducible representations are known to exist: Δ_1, Δ_2 and Δ_3 (refs. 20,28). The labels of the irreducible representations are based on the convention in ref. 28. The Γ_1 and Γ_2 modes at the Γ point change to the Δ_1 mode, whereas the Γ_3 modes split into Δ_2 and Δ_3 modes in accordance with the compatibility relations. In Supplementary Note 1, we present a derivation of the Raman tensors that correspond to the Δ_2 and Δ_3 modes. It follows that the Raman intensities of the Δ_2 and Δ_3 modes are in the ratio of $I_{RR}:I_{LL}:I_{RL}:I_{LR}$ = 0:0:1:0 and 0:0:0:1, respectively. This is consistent with the results of the Raman experiments. In other words, spin PAM $m^{s}_{PAM}(RH) = 0$, +1 and −1 correspond to Δ_1, Δ_2 and Δ_3, respectively, because the phase change by three-fold rotation is the index of each irreducible representation. For L-HgS, $m^{s}_{PAM}(LH) = 0$, +1 and −1 correspond to Δ_1, Δ_3 and Δ_2, respectively[28].

Finally, we discuss the propagation of the chiral phonons. From Fig. 3, the group velocities of the $\Gamma_3^{(1-5)}$ modes at the N point are calculated to be approximately $\pm(0.4–2) \times 10^3$ m s^{-1}, which is comparable to the sound velocity of acoustic phonons. Note that the nonreciprocal propagation of chiral phonons can be controlled by the PAM of the photon. This implies the possibility of transferring the PAM from photons to electron spins via propagating chiral phonons in opto-phononic-spintronic devices. For example, taking advantage of the long coherence of long-wavelength phonons, transferring the PAM from phonon to electron spins may be realized on the macroscopic scale.

Weyl phonons can exist widely in chiral crystals, as has been predicted by the first-principles calculations and verified by inelastic X-ray scattering[29,30]. Note that the circularly polarized Raman spectroscopy presented in this paper may open the possibility to detect phonons carrying a non-zero Chern number by measuring the phonon PAM, instead of detecting the eigenvalue and eigenvectors of the topological bands.

We observed chiral phonons in a three-dimensional chiral system using circularly polarized Raman spectroscopy and first-principles calculations. The chiral phonons were labelled with spin PAM of {+1, −1} corresponding to {Δ_2, Δ_3} and {Δ_3, Δ_2} for R- and L-HgS, respectively, with opposite group velocities of ~1 km s^{-1}. The parity and time-reversal symmetries of the phonons satisfy the definition of truly chiral phonons, which propagate while rotating along the *c* axis. This is distinct from the chiral phonons observed in two-dimensional hexagonal systems. Our work also provides an optical method to identify the handedness of chiral materials using PAM, and we demonstrated that spatial imaging of chiral domains can be achieved in a non-contact and non-destructive manner.

Online content

Any methods, additional references, Nature Research reporting summaries, source data, extended data, supplementary information, acknowledgements, peer review information; details of author contributions and competing interests; and statements of data and code availability are available at https://doi.org/10.1038/s41567-022-01790-x.

References

1. Kelvin, W. T. B. *Baltimore Lectures on Molecular Dynamics and the Wave Theory of Light* (Cambridge Univ. Press, 1904).
2. Cahn, R. S., Ingold, C. & Prelog, V. Specification of molecular chirality. *Angew. Chem. Int. Ed. Engl.* **5**, 385–415 (1966).
3. Barron, L. D. *Molecular Light Scattering and Optical Activity* 2nd edn (Cambridge Univ. Press, 2004).
4. Božovic, I. Possible band-structure shapes of quasi-one-dimensional solids. *Phys. Rev. B* **29**, 6586–6599 (1984).
5. Zhang, L. & Niu, Q. Chiral phonons at high-symmetry points in monolayer hexagonal lattices. *Phys. Rev. Lett.* **115**, 115502 (2015).
6. Chen, H., Zhang, W., Niu, Q. & Zhang, L. Chiral phonons in two-dimensional materials. *2D Mater.* **6**, 012002 (2019).
7. Zhu, H. et al. Observation of chiral phonons. *Science* **359**, 579–582 (2018).
8. Kishine, J., Ovchinnikov, A. S. & Tereshchenko, A. A. Chirality-induced phonon dispersion in a noncentrosymmetric micropolar crystal. *Phys. Rev. Lett.* **125**, 245302 (2020).
9. Pine, A. S. & Dresselhaus, G. Linear wave-vector shifts in the Raman spectrum of α-quartz and infrared optical activity. *Phys. Rev.* **188**, 1489–1496 (1969).
10. Zallen, R., Lucovsky, G., Taylor, W., Pinczuk, A. & Burstein, E. Lattice vibrations in trigonal HgS. *Phys. Rev. B* **1**, 4058–4070 (1970).

11. Pine, A. S. & Dresselhaus, G. Raman spectra and lattice dynamics of tellurium. *Phys. Rev. B* **4**, 356–371 (1971).
12. Grimsditch, M. H., Ramdas, A. K., Rodriguez, S. & Tekippe, V. J. Piezospectroscopy of Raman lines exhibiting linear wave-vector dependence: α-quartz. *Phys. Rev. B* **15**, 5869–5876 (1977).
13. Imaino, W., Simpson, C. T., Becker, W. M. & Ramdas, A. K. Resonant Raman effect in cinnabar. *Phys. Rev. B* **21**, 634–642 (1980).
14. Garasevich, S. G., Slobodyanyuk, A. V. & Yanchuk, Z. Z. Anomalous angular dependence of E-mode splitting in Raman spectra of ZnP_2 and CdP_2 uniaxial gyrotropic crystals caused by spatial dispersion. *Phys. Lett. A* **197**, 238–242 (1995).
15. Pinan-Lucarre, J.-P., Ouillon, R. & Ranson, P. Linear wave vector dependence of low-frequency Raman modes in two uniaxial gyrotropic quartz-type materials: α-$GaPO_4$ and α-$AlPO_4$. *Chem. Phys. Lett.* **302**, 164–170 (1999).
16. Cardona, M. et al. Electronic and phononic properties of cinnabar: ab initio calculations and some experimental results. *Phys. Rev. B* **82**, 085210 (2010).
17. Aurivillius, K. L. On the crystal structure of cinnabar. *Acta Chem. Scand.* **4**, 1413–1436 (1950).
18. Glazer, A. M. & Stadnicka, K. On the origin of optical activity in crystal structures. *J. Appl. Cryst.* **19**, 108–122 (1986).
19. Higgs, P. W. The vibration spectra of helical molecules: infra-red and Raman selection rules, intensities and approximate frequencies. *Proc. Math. Phys. Eng. Sci.* **220**, 472–485 (1953).
20. Nusimovici, M. A. & Gorre, G. Phonons in cinnabar. *Phys. Rev. B* **8**, 1648–1656 (1973).
21. Bond, W. L., Boyd, G. D. & Carter Jr, H. L. Refractive indices of HgS (cinnabar) between 0.62 and 11 μ. *J. Appl. Phys.* **38**, 4090–4091 (1967).
22. Nussbaum, A. & Hager, R. J. Galvanomagnetic coefficients of single-crystal tellurium. *Phys. Rev.* **123**, 1958–1964 (1961).
23. Yariv, A. & Yeh, P. *Photonics: Optical Electronics in Modern Communications* 6th edn (Oxford Univ. Press, 2006).
24. Bloembergen, N. Conservation laws in nonlinear optics. *J. Opt. Soc. Am.* **70**, 1429–1436 (1980).
25. Tatsumi, Y., Kaneko, T. & Saito, R. Conservation law of angular momentum in helicity-dependent Raman and Rayleigh scattering. *Phys. Rev. B* **97**, 195444 (2018).
26. Chen, H., Wu, W., Zhu, J., Yang, S. A. & Zhang, L. Propagating chiral phonons in three-dimensional materials. *Nano Lett.* **21**, 3060–3065 (2021).
27. Zhang, T. & Murakami, S. Chiral phonons and pseudoangular momentum in nonsymmorphic systems. *Phys. Rev. Res.* **4**, L012024 (2022).
28. Teuchert, W. D. & Geick, R. Symmetry of lattice vibrations in selenium and tellurium. *Phys. Stat. Sol. B* **61**, 123–136 (1974).
29. Zhang, T. et al. Double-Weyl phonons in transition-metal monosilicides. *Phys. Rev. Lett.* **120**, 016401 (2018).
30. Li, H. et al. Observation of a chiral wave function in the twofold-degenerate quadruple Weyl system BaPtGe. *Phys. Rev. B* **103**, 184301 (2021).

Methods

Raman scattering

We used a custom-built Raman spectroscopy system[31] equipped with a monochromator, charge-coupled device camera and optical elements. Details of the setup can be found in Supplementary Fig. 2. The excitation light was generated by a diode laser with a wavelength of $\lambda = 785$ nm. The incident and scattered light were propagated along the c axis of the crystal. All the measurements were performed at room temperature.

First-principles calculations

First-principles calculations were performed using the ABINIT package[32,33], which implements density functional perturbation theory[34]. An anaddb code was used to obtain the phonon dispersion curve[35,36]. For the calculation of the phonon dispersion, the exchange-correlation energy of electrons is described in the generalized gradient approximation with norm-conserving pseudo-potentials[37,38], and spin–orbit coupling was not considered. We set the kinetic energy cut-off to 60 Ha, which was necessary to obtain a well-converged result, and the wave vector $\mathbf{k}$ grids of $6 \times 6 \times 4$ to describe the phonon dispersion curve. In addition, we increased the precision of the $\mathbf{k}$ grids to $8 \times 8 \times 8$ to obtain the converged phonon frequency at the Γ point. The following lattice parameters of α-HgS were used: cell volume of $V_0 = 160.02$ Å^3, cell lengths of $a = 4.11$ Å, $b = 4.11$ Å and $c = 9.40$ Å, and cell angles of $\alpha = 90^\circ$, $\beta = 90^\circ$, and $\gamma = 120^\circ$ (refs. 39,40). R-HgS is composed of three Hg atoms at (0.699, 0.699, 0.000), (0.000, 0.301, 2/3) and (0.301, 0.000, 1/3) and three S atoms at (0.509, 0.509, 1/2), (0.000, 0.491, 1/6) and (0.491, 0.000, 5/6), whereas L-HgS is composed of three Hg atoms at (0.699, 0.699, 0.000), (0.301, 0.000, 2/3) and (0.000, 0.301, 1/3) and three S atoms at (0.509, 0.509, 1/2), (0.491, 0.000, 1/6) and (0.000, 0.491, 5/6), of which the bases are the a, b and c components. The essential part of the ABINIT results was confirmed using the VASP package.

Calculation of PAM

In a material with three-fold rotational symmetry, PAM is defined as[5,4]

$$\{C_3 \mid 0\}\,\mathbf{u}(\mathbf{k}) = \exp\left[-\mathrm{i}\frac{2\pi}{3} m_{\mathrm{PAM}}(\mathbf{k})\right]\mathbf{u}(\mathbf{k}), \tag{2}$$

where $m_{\mathrm{PAM}}(\mathbf{k})$ is the PAM of phonons, $\mathbf{u}(\mathbf{k})$ is the displacement vector and $\{C_3 \mid 0\}$ is the three-fold rotation around the c axis. However, α-HgS has a three-fold helical rotational symmetry instead of a three-fold rotational symmetry. Therefore, we defined the PAM of phonons in R- and L-HgS as[27]

$$\{C_3 \mid \mathbf{c}/3\}\,\mathbf{u}(\mathrm{RH}, \mathbf{k}) = \exp\left[-\mathrm{i}\frac{2\pi}{3} m_{\mathrm{PAM}}(\mathrm{RH}, \mathbf{k})\right]\mathbf{u}(\mathrm{RH}, \mathbf{k}), \tag{3}$$

$$\{C_3 \mid 2\mathbf{c}/3\}\,\mathbf{u}(\mathrm{LH}, \mathbf{k}) = \exp\left[-\mathrm{i}\frac{2\pi}{3} m_{\mathrm{PAM}}(\mathrm{LH}, \mathbf{k})\right]\mathbf{u}(\mathrm{LH}, \mathbf{k}), \tag{4}$$

where $\{C_3 \mid \mathbf{c}/3\}$ and $\{C_3 \mid 2\mathbf{c}/3\}$ are combinations of the three-fold rotation around the c axis and the $c/3$ and $2c/3$ translations along the c axis, respectively.

The displacement vector of phonons can be expressed as

$$\mathbf{u}_\kappa(\mathbf{k}, l, j) = m_\kappa^{-\frac{1}{2}} \boldsymbol{\epsilon}_\kappa(\mathbf{k}, j) \exp\left[\mathrm{i}\left\{\mathbf{k}\cdot\mathbf{R}_l - \omega(\mathbf{k}, j)t\right\}\right], \tag{5}$$

where j is the number of phonon modes, m_κ is the mass of the κth atom in the lth unit cell, $\boldsymbol{\epsilon}_\kappa(\mathbf{k}, j)$ is the eigenvector of the dynamical matrix and $\mathbf{R}_l$ is the position of the lth unit cell. The use of equation (5) indicates that the phase of the eigenvector consists of two parts: $\boldsymbol{\epsilon}(\mathbf{k})$ and $\exp[\mathrm{i}\mathbf{k}\cdot\mathbf{R}_l]$, both of which contribute to the calculation of the PAM. In the former, the phase difference of $\boldsymbol{\epsilon}(\mathbf{k})$ leads to the spin PAM $m^{\mathrm{s}}_{\mathrm{PAM}}$, which is quantized as an integer. The latter factor, $\exp[\mathrm{i}\mathbf{k}\cdot\mathbf{R}_l]$, provides the orbital PAM $m^{\mathrm{o}}_{\mathrm{PAM}}$, which is therefore equal to $\frac{1}{2\pi}\mathbf{k}\cdot\mathbf{c}$ under a three-fold helical rotation. Consequently, for each wavenumber $\mathbf{k}$, the total PAM is

$$m_{\mathrm{PAM}} = m^{\mathrm{s}}_{\mathrm{PAM}} + m^{\mathrm{o}}_{\mathrm{PAM}}. \tag{6}$$

Here we considered only the spin PAM in the phonon dispersion, as shown in Fig. 3a.

Calculation of AM

The AM of phonons at wavenumber $\mathbf{k}$ of mode number j is defined as[41]

$$m_{\mathrm{AM}}(\mathbf{k}, j) = \left(\boldsymbol{\epsilon}(\mathbf{k}, j)^\dagger M \boldsymbol{\epsilon}(\mathbf{k}, j)\right)\hbar, \tag{7}$$

where $M = \begin{pmatrix} 0 & -i & 0 \\ i & 0 & 0 \\ 0 & 0 & 0 \end{pmatrix} \otimes I_{n\times n}$, where the basis of the 3×3 matrix is represented using the orthogonal bases (u_x, u_y, u_z), n is the number of atoms in a unit cell and $I_{n\times n}$ is a unit matrix of $n \times n$. The eigenvector of the dynamical matrix $\boldsymbol{\epsilon}(\mathbf{k}, j)$ is normalized as

$$\boldsymbol{\epsilon}(\mathbf{k}, j)^\dagger \boldsymbol{\epsilon}(\mathbf{k}, j) = 1. \tag{8}$$

The origin of spin and orbital PAMs

Here we provide an explicit form of the spin and orbital PAMs associated with the helical operation $\{C_3 \mid \mathbf{c}/3\}$, where $\mathbf{c}/3$ is the non-primitive translation. The atomic displacement vector field $\mathbf{u}_\mathbf{k}(\mathbf{r})$ associated with the phonon propagation may be generally written as

$$\mathbf{u}_\mathbf{k}(\mathbf{r}) = \boldsymbol{\epsilon}(\mathbf{k}) \exp(\mathrm{i}\mathbf{k}\cdot\mathbf{r}). \tag{9}$$

Then, $\mathbf{u}_\mathbf{k}(\mathbf{r})$ is transformed in accordance with a general rule

$$\{C_3 \mid \mathbf{c}/3\}\,\mathbf{u}_\mathbf{k}(\mathbf{r}) = \left[C_3\boldsymbol{\epsilon}(\mathbf{k})\right] \exp\left(\mathrm{i}\mathbf{k}\cdot\{C_3|\mathbf{c}/3\}^{-1}\mathbf{r}\right). \tag{10}$$

Note that $\{C_3|\mathbf{c}/3\}^{-1} = \left\{C_3^{-1} \mid -C_3^{-1}\mathbf{c}/3\right\}$, $\mathbf{k}\cdot\mathbf{r}$ is a scalar and $C_3\boldsymbol{\epsilon}(\mathbf{k}) = \exp\left(-\mathrm{i}\frac{2\pi}{3}m\right)\boldsymbol{\epsilon}(\mathbf{k})$, thus we have

$$\{C_3 \mid \mathbf{c}/3\}\,\mathbf{u}_\mathbf{k}(\mathbf{r}) = \exp\left[-\mathrm{i}\frac{2\pi}{3}\left(m^{\mathrm{s}}_{\mathrm{PAM}} + m^{\mathrm{o}}_{\mathrm{PAM}}\right)\right]\mathbf{u}_\mathbf{k}(\mathbf{r}), \tag{11}$$

where the respective spin and orbital PAMs are introduced as

$$m^{\mathrm{s}}_{\mathrm{PAM}} = m, \tag{12}$$

and

$$m^{\mathrm{o}}_{\mathrm{PAM}} = -\frac{3}{2\pi}\left\{(C_3\mathbf{k}) - \mathbf{k}\right\}\cdot\mathbf{r} + \frac{1}{2\pi}(C_3\mathbf{k})\cdot\mathbf{c}, \tag{13}$$

which yield the total PAM, $m_{\mathrm{PAM}} = m^{\mathrm{s}}_{\mathrm{PAM}} + m^{\mathrm{o}}_{\mathrm{PAM}}$.

In this study, we consider the path Δ from Γ to A, where $C_3\mathbf{k} = \mathbf{k}$ denotes the modulo reciprocal lattice vectors. Thus, $m^{\mathrm{o}}_{\mathrm{PAM}} = \frac{1}{2\pi}\mathbf{k}\cdot\mathbf{c}$. The same symmetry properties apply to the photons propagating along the helical axis. Then, we obtain the selection rule in equation (1), which includes only $m^{\mathrm{s}}_{\mathrm{PAM}}$, by cancelling out the $m^{\mathrm{o}}_{\mathrm{PAM}}$ terms because of the law of conservation of momentum.

Data availability

Source data are provided with this paper.

Code availability

All custom codes used for the data processing and numerical simulations are available from the corresponding author upon reasonable request.

References

31. Hsu, W.-H., Shen, K., Fujii, Y., Koreeda, A. & Satoh, T. Observation of terahertz magnon of Kaplan–Kittel exchange resonance in yttrium-iron garnet by Raman spectroscopy. *Phys. Rev. B* **102**, 174432 (2020).
32. Gonze, X. et al. ABINIT: first-principles approach to material and nanosystem properties. *Comput. Phys. Commun.* **180**, 2582–2615 (2009).
33. Romero, A. H. et al. ABINIT: overview, and focus on selected capabilities. *J. Chem. Phys.* **152**, 124102 (2020).
34. Hamann, D. R., Wu, X., Rabe, K. M. & Vanderbilt, D. Metric tensor formulation of strain in density-functional perturbation theory. *Phys. Rev. B* **71**, 035117 (2005).
35. Gonze, X. First-principles responses of solids to atomic displacements and homogeneous electric fields: implementation of a conjugate-gradient algorithm. *Phys. Rev. B* **55**, 10337–10354 (1997).
36. Gonze, X. & Lee, C. Dynamical matrices, Born effective charges, dielectric permittivity tensors, and interatomic force constants from density-functional perturbation theory. *Phys. Rev. B* **55**, 10355–10368 (1997).
37. van Setten, M. J. et al. The PseudoDojo: training and grading a 85 element optimized norm-conserving pseudopotential table. *Comput. Phys. Commun.* **226**, 39–54 (2018).
38. Hamann, D. R. Optimized norm-conserving Vanderbilt pseudopotentials. *Phys. Rev. B* **88**, 085117 (2013).
39. Jain, A. et al. Commentary: The Materials project: a materials genome approach to accelerating materials innovation. *APL Mater.* **1**, 011002 (2013).
40. Rodic, D., Spasojevic, V., Bajorek, A. & Onnerud, P. Similarity of structure properties of $Hg_{1-x}Mn_xS$ and $Cd_{1-x}Mn_xS$ (structure properties of HgMnS and CdMnS). *J. Magn. Magn. Mater.* **152**, 159–164 (1996).
41. Zhang, L. & Niu, Q. Angular momentum of phonons and the Einstein–de Haas effect. *Phys. Rev. Lett.* **112**, 085503 (2014).

Acknowledgements

We thank M. Kichise, A. Kawano, K. Matsumoto, A. Koreeda, Y. Fujii, E. Oishi and H. M. Yamamoto for valuable discussions and technical support. T.S. was supported financially by the Japan Society for the Promotion of Science KAKENHI (grant nos. JP19H01828, JP19H05618, JP19K21854, JP21H01032 and JP22H01154) and the Frontier Photonic Sciences Project of the National Institutes of Natural Sciences (grant nos. 01212002 and 01213004).

Author contributions

T.S. and J.K. conceived the study. K.I. and H.M. performed the Raman experiments. Y.K., Y.T. and S.I. conducted the X-ray analyses. K.I., H.M., T.Z. and S.M. performed the first-principles calculations. K.I., H.M., J.K. and T.S. wrote the manuscript. All authors discussed the results and commented on the manuscript.

Competing interests

The authors declare no competing interests.

Additional information

Extended data is available for this paper at https://doi.org/10.1038/s41567-022-01790-x.

Supplementary information The online version contains supplementary material available at https://doi.org/10.1038/s41567-022-01790-x.

Correspondence and requests for materials should be addressed to Takuya Satoh.

Peer review information *Nature Physics* thanks Przemyslaw Piekarz and the other, anonymous, reviewer(s) for their contribution to the peer review of this work. This article has been peer reviewed as part of Springer Nature's Guided Open Access initiative.

https://doi.org/10.1038/s41567-022-01790-x

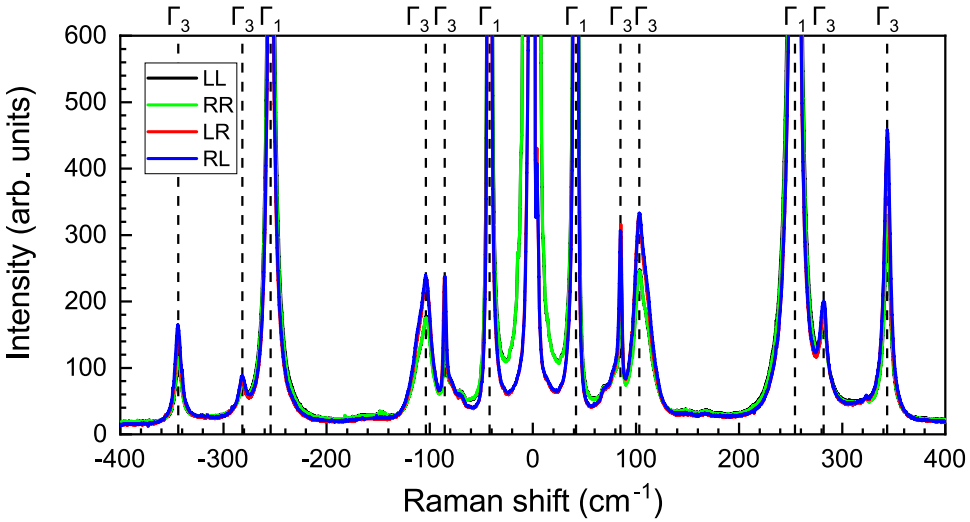

Extended Data Fig. 1 | Full Raman spectra of R-HgS. Full Raman spectra were recorded at room temperature using various polarized configurations. The black, green, red and blue spectra represent the LL-, RR-, LR- and RL-polarized configurations, respectively. R and L represent the right- and left-handed helicities of circularly polarized light, respectively.

https://doi.org/10.1038/s41567-022-01790-x

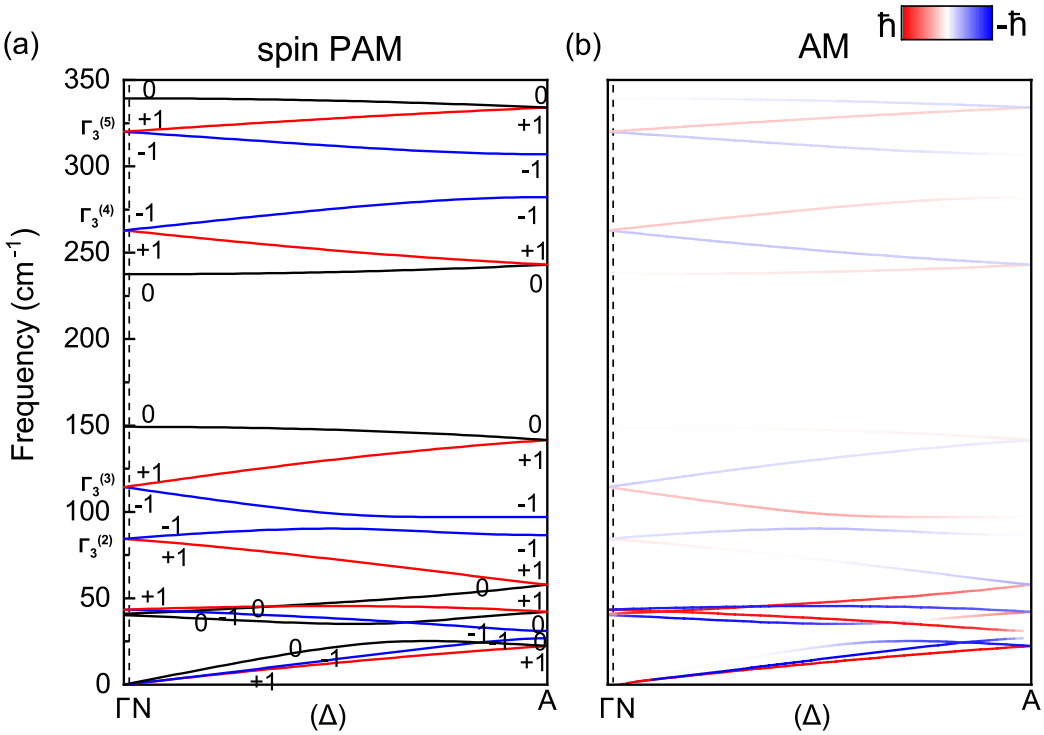

Extended Data Fig. 2 | Dispersion of L-HgS along the left-handed helical axis. (a) Phonon dispersion curves for spin PAM $m^{s}_{PAM} = 0$ (black), $+1$ (red) and -1 (blue). (b) Phonon AM along the helical axis, denoted by the colour gradient. Red and blue curves correspond to the positive and negative AM, respectively.

https://doi.org/10.1038/s41567-022-01790-x

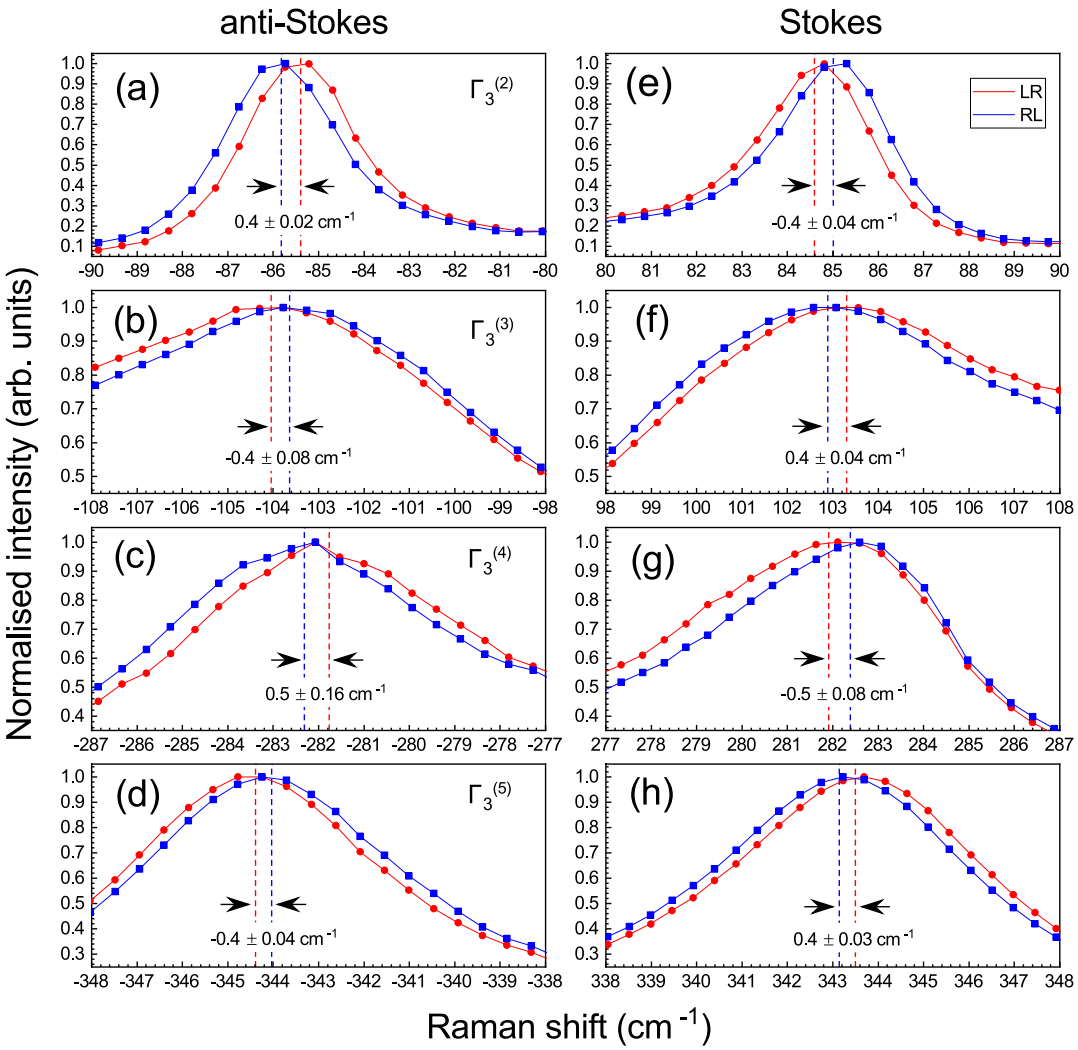

Extended Data Fig. 3 | Raman spectra of *α*-HgS with unknown chirality. (a–h), Anti-Stokes (a–d) and Stokes (e–h) spectra of the $\Gamma_3^{(2)}$ (a,e), $\Gamma_3^{(3)}$ (b,f), $\Gamma_3^{(4)}$ (c,g) and $\Gamma_3^{(5)}$ (d,h) modes, along with the Γ_3 modes observed experimentally with RL- (blue line) and LR-polarized (red line) configurations and the Γ_3 doublet splittings (dashed vertical lines) in (a–h). The error values take into account that multiple splitting measurements were conducted in the experiment, owing to the roughness of the sample surface.

https://doi.org/10.1038/s41567-022-01790-x

Symmetry	Our experiments	Experiments [10]	Our calculations	Calculations [16]
$\Gamma^{(1)}_{2,\mathrm{LO}}$	Inactive		40.2	44.1
$\Gamma^{(1)}_{1}$	42	45	41.0	39.1
$\Gamma^{(1)}_{3,\mathrm{TO}}$			43.5	42.0
$\Gamma^{(2)}_{3,\mathrm{TO}}$	85	88	84.4	83.1
$\Gamma^{(3)}_{3,\mathrm{TO}}$	103	106	114.4	121.4
$\Gamma^{(2)}_{2,\mathrm{LO}}$	Inactive		149.4	159.6
$\Gamma^{(2)}_{1}$	254	256	237.5	232.1
$\Gamma^{(4)}_{3,\mathrm{TO}}$	282	283	263.0	259.3
$\Gamma^{(5)}_{3,\mathrm{TO}}$	344	345	320.2	319.2
$\Gamma^{(3)}_{2,\mathrm{LO}}$	Inactive		339.4	337.7

Extended Data Table 1 | phonon frequencies in α-HgS. The experimental values in cm^{-1} were obtained at room temperature. The calculated values in cm^{-1} are at the Γ point.

https://doi.org/10.1038/s41567-022-01790-x

	Experiment			Calculation				
Symmetry at Γ point	Config.	Frequency [cm^{-1}]	Splitting [cm^{-1}]	Symmetry at N point	Frequency [cm^{-1}]	Splitting [cm^{-1}]	m^{s}_{PAM}	m_{AM}
$\Gamma_3^{(2)}$	RL	84.9	0.3 ± 0.01	$\Delta_3^{(2)}$	84.2	0.4	-1	$-$
	LR	85.3		$\Delta_2^{(2)}$	84.6		$+1$	$+$
$\Gamma_3^{(3)}$	LR	103.2	0.3 ± 0.16	$\Delta_2^{(3)}$	114.0	0.9	$+1$	$-$
	RL	103.5		$\Delta_3^{(3)}$	114.9		-1	$+$
$\Gamma_3^{(4)}$	RL	281.9	0.4 ± 0.08	$\Delta_3^{(4)}$	262.7	0.7	-1	$+$
	LR	282.3		$\Delta_2^{(4)}$	263.4		$+1$	$-$
$\Gamma_3^{(5)}$	LR	343.5	0.3 ± 0.05	$\Delta_2^{(5)}$	320.0	0.4	$+1$	$+$
	RL	343.7		$\Delta_3^{(5)}$	320.4		-1	$-$

Extended Data Table 2 | Chiral properties of phonons in R-HgS along the right-handed helical axis. Owing to the roughness of the sample surface, multiple splitting measurements were conducted, with the deviation indicated by the error values.

https://doi.org/10.1038/s41567-022-01790-x

	Experiment			Calculation				
Symmetry at Γ point	Config.	Frequency [cm^{-1}]	Splitting [cm^{-1}]	Symmetry at N point	Frequency [cm^{-1}]	Splitting [cm^{-1}]	m^{s}_{PAM}	m_{AM}
$\Gamma_3^{(2)}$	LR	84.6	0.4 ± 0.04	$\Delta_3^{(2)}$	84.2	0.4	$+1$	$+$
	RL	85.0		$\Delta_2^{(2)}$	84.6		-1	$-$
$\Gamma_3^{(3)}$	RL	102.9	0.4 ± 0.04	$\Delta_2^{(3)}$	114.0	0.9	-1	$+$
	LR	103.3		$\Delta_3^{(3)}$	114.9		$+1$	$-$
$\Gamma_3^{(4)}$	LR	281.9	0.5 ± 0.08	$\Delta_3^{(4)}$	262.7	0.7	$+1$	$-$
	RL	282.4		$\Delta_2^{(4)}$	263.4		-1	$+$
$\Gamma_3^{(5)}$	RL	343.1	0.4 ± 0.03	$\Delta_2^{(5)}$	320.0	0.4	-1	$-$
	LR	343.5		$\Delta_3^{(5)}$	320.4		$+1$	$+$

Extended Data Table 3 | Chiral properties of phonons in α-HgS with unknown chirality. The error values take into account that multiple splitting measurements were conducted in the experiment, owing to the roughness of the sample surface. Calculations were performed for L-HgS.